

3D femtosecond laser patterning of collagen for directed cell attachment

Yaoming Liu^a, Shan Sun^b, Sima Singha^a, Michael R. Cho^b, Robert J. Gordon^{a,*}

^aDepartment of Chemistry (m/c 111), University of Illinois at Chicago, 845 W Taylor Street, Chicago, IL 60607, USA

^bDepartment of Bioengineering (m/c 063), University of Illinois at Chicago, Chicago, IL 60607, USA

Received 31 August 2004; accepted 13 November 2004

Abstract

Three-dimensional micropatterned collagen scaffolds were fabricated by femtosecond laser ablation. An 800 nm, 45 fs Ti:Sapphire laser was used to create various 3D patterns in a collagen gel, including holes, lines and grids. An optimal collagen concentration was found for both substrate patterning and cell compatibility. The threshold fluence for ablation of the scaffold was found to be 0.06 J/cm², and the morphology of the ablation craters was measured as a function of fluence. Mesenchymal stem cells from rat bone marrow and human fibroblasts were seeded within the ablated patterns and were shown to be viable for at least 10 days. © 2004 Elsevier Ltd. All rights reserved.

Keywords: Cell adhesion; Collagen; Laser ablation; Micropatterning; Tissue engineering

1. Introduction

The size, shape, alignment, and orientation of cells are influenced by their local environment. The topography and composition of the extra-cellular matrix affect cellular functions, such as adhesion, growth, motility, secretion, gene expression, and apoptosis. Controlling this environment is therefore essential in designing scaffolds for tissue engineering [1]. The scaffold should be biocompatible; its structure should have the mechanical strength needed to support growing and contracting tissue, yet be sufficiently porous and permeable to transport nutrients and waste; its surfaces should have the proper physical and chemical properties to promote cell adhesion and growth. Channels and ridges in the scaffold promote contact guidance to orient cells, providing the organization and mechanical strength required by healthy tissue [2]. Three-dimensional cell

structures are also valuable for providing in vitro models for studying diseased cell–cell interactions [3].

Collagen is a preferred scaffolding material for a variety of reasons [4]. Amounting to 25% of the body protein, it is a good host for many different types of cells. Cross-linking gives it mechanical strength and promotes the formation of fibers, fibrils, and macroscopic bundles. Implanted collagen provokes a minimal immunoreactive response, and its eventual biodegradation mimics normal wound healing.

Creating three-dimensional structures in scaffolding material with micron resolution is a challenge in biomaterial design [5]. Many of the existing fabrication techniques mimic processes used in the microelectronics industry. The four main methods used are photolithography, soft lithography, direct writing, and laser ablation. Photolithography is not immediately suitable for 3D fabrication, and, in addition, suffers from a number of drawbacks, including the need for a clean room, the cost of mask fabrication, and the biotoxicity of the resist and developer solution. Soft lithography, a group of techniques developed by Whitesides and coworkers [6], overcomes many of the limitations of

*Corresponding author. Tel.: +1 312 996 3280; fax: +1 312 996 0431.

E-mail address: rjgordon@uic.edu (R.J. Gordon).

photolithography. These techniques rely on using a transparent elastomer (PDMS), patterned as a bas-relief stamp, to transfer a protein pattern to a suitable substrate, to which cells can then adhere. Soft lithography includes microcontact printing, which is the more widely used technique, and microfluidic patterning, in which fluids are restricted to non-contact regions. Variants of soft lithography have been applied by several laboratories to create 3D patterns and to study cell pattern integrity in 3D environments [7–12].

In a third approach, which we loosely term “direct writing,” material is deposited directly onto a substrate without a pressure contact. Examples in order of decreasing resolution are (i) dip-pen lithography, which uses atomic force microscopy (AFM) techniques to deposit single protein molecules with 30 nm resolution [13], (ii) laser-guided direct-writing, which uses the dipole force to deposit micron size particles [14], (iii) extrusion of a polymer (PLGA) through a computer-controlled microsyringe to build up patterns with 5–10 μm resolution [15], and (iv) inkjet printing of collagen with a minimum feature size of 350 μm [16]. The latter two methods produce 3D structures, though with pattern complexities that are limited by the methodology.

The fourth method, which is the subject of the present paper, is laser ablation. The advantages of this approach include its very high resolution (down to 25 nm [17]), non-contact interaction, and applicability to any substrate. From the present perspective, the most important characteristic distinguishing different laser sources is the time scale of the interaction. The critical periods are the thermal and mechanical relaxation times of the substrate, which are on the sub-nanosecond time scale. The vast majority of applications of lasers to biological and medical material processing have used long pulse (>10 ns) or continuous wave lasers [18]. Examples of 2D applications of such lasers to tissue engineering are patterning of cell growth by localized ablation of adhesion-inhibiting polymers [19] and the fabrication of grooves to enhance cell adhesion [20], both using a photomask to achieve micron resolution. Complex micropatterns of biological molecules may be deposited on surfaces by selective adsorption on laser-ablated patterns of self-assembled monolayers [21].

Femtosecond (1 fs = 10^{-15} s) lasers have several distinct advantages for material processing. Ablation with intense pulses is induced by optical breakdown, which generates a plasma at the focal point of the laser. Because the plasma recombines before thermal diffusion, shock wave propagation, and cavitation set in, ablation of the substrate is confined, at least initially, to a small volume. Although the intensity required to initiate breakdown is fairly high (10^{13} W/cm² at 100 fs in water [18]), the short duration of the pulse allows the threshold intensity to be achieved with a modest fluence

(1 J/cm² in this case [18]). The combination of localized excitation and low threshold fluence can greatly reduce the extent of collateral damage to surrounding areas. For pulses shorter than ~ 20 ps, electrons are heated and chemical bonds are broken before the electrons have time to transfer their energy to the matrix [22]. In contrast, for nanosecond and longer pulses, thermal and mechanical propagation occur during the irradiation, causing melting and vaporization far from the absorption site, and resolidification of the melt zone also affects the precision and quality of the laser machining. The advantages of fs laser ablation have been exploited, for example, in refractive surgery [23] and all-optical histology of brain tissue [24]. Another important characteristic of fs laser ablation is that the plasma is initiated by multiphoton absorption. This property allows ablation to occur in materials that are transparent at the laser wavelength, producing bulk modification localized near the focal point [25].

In the present paper, we report the first application of ultrashort laser pulses to the 3D patterning of tissue scaffolds. We present results on the ablation morphology of collagen by 50–75 fs, 800 nm laser pulses, and demonstrate the viable growth of mesenchymal stem cells and fibroblasts in the ablated structures.

2. Materials and methods

2.1. Experimental setup

A train of 45 fs pulses is generated by a Ti:Sapphire oscillator (Spectra-Physics Tsunami oscillator pumped by a Millennia diode laser). These pulses are amplified by a Ti:Sapphire regenerative amplifier (Spectra-Physics Spitfire 50FS, pumped by an Evolution 30 Nd:YLF laser). The output of this laser system is a 1 kHz train of 45 fs, 2 mJ pulses, with a peak wavelength of 800 nm and a FWHM bandwidth of 40 nm. The number of pulses in the train is controlled externally by sending trigger signals to the Pockels cell of the amplifier. The trigger pulses are initiated by a MATLAB computer program, which controls the irradiation time with ms precision.

The energy of the laser pulses was attenuated by a Rochon polarizer followed by a half-wave plate. The attenuated laser beam was steered by a pair of mirrors and a periscope into the objective of a modified light microscope (AO Spencer 1051, with $10\times/0.25$ NA objective), which focuses the radiation onto the sample. The pulse energy was measured after the microscope optics with an Ophir 2A-SH power meter. The spatial profile of the laser beam was characterized by sliding a knife edge across the beam, while measuring the transmitted light with a photodiode. We estimate that the microscope objective temporally stretches the pulse to ~ 50 fs, and that the objective plus beam-splitter

(inserted to transmit an image to the eyepiece) stretches it to ~ 75 fs.

The target material was placed on a high-resolution ($0.5\ \mu\text{m}$) 3D translation stage. Micropatterns were produced in the sample by moving the stage while the laser was firing.

2.2. Collagen preparation

Collagen gel was formed at physiological conditions (pH 7.4, osmolarity 0.3 osm/L) by mixing 50% type I collagen from rat tail (BD Biosciences), 40% 0.1 M NaOH, 10% 10 \times concentrated Hank's buffer salt solution (HBSS), and 0.02% glutaraldehyde (GTA) added in bulk as a cross-linking agent before the gel solidified. Previous studies showed the onset of significant GTA cytotoxicity at concentrations $>0.05\%$ [26,27]. The 1 mM concentration of L-lysine in the cell medium (see Section 2.3) helped further reduce the GTA cytotoxicity [27]. The gel solution was placed into a rubber ring (8 mm high, 12.7 mm I.D.) cut from polyurethane tubing, with one end mounted on a cover slip. The gel was incubated overnight at 37°C and then soaked in Dulbecco's phosphate-buffered saline (DPBS) to remove any residual cross-linking agent. A typical sample was a round disc, 10 mm in diameter and 1–2 mm in thickness. Different concentrations of collagen were tested. A final concentration of 2 mg/mL was found to be optimal both for laser micropatterning and cell growth.

2.3. Cell seeding

The laser-patterned collagen blocks were rinsed with DPBS before the introduction of cells. A 1 mL microliter syringe was used to place a suspension of either mesenchymal stem cells isolated from rat bone marrow or of human HT1080 fibroblasts (obtained from ATCC) onto the top surface of a collagen disk. The surface was washed with Dulbecco's minimum essential medium (DMEM) 1 min after addition of the cell suspension in order to confine the cells within the patterned sites and to prevent them from attaching to the gel surface. The medium was supplemented with 10% fetal bovine serum (FBS) and 1% antibiotics/antimycotics (final concentration: penicillin 100 units/mL, streptomycin 100 mg/mL, and amphotericin B 0.25 mg/mL). A fresh amount of enriched DMEM was subsequently added to the sample, which was returned to the 37°C incubator (containing 95% humidified air and 5% CO_2) for later use.

2.4. Cell viability

Cells were loaded with $2\ \mu\text{M}$ calcein-AM and $4\ \mu\text{M}$ ethidium homodimer for 30 min in an incubator and observed using fluorescence microscopy. Green

fluorescence results when calcein-AM is hydrolyzed and retained by living cells. Red fluorescence indicates dead cells, because ethidium homodimer is membrane permeant only in dead cells.

2.5. Microscopy

The laser ablation patterns formed in the collagen scaffold and the cells growing within the sculpted patterns were observed with a Nikon Eclipse E800 upright microscope, equipped with a $20\times/0.75$ objective lens. 3D images were acquired by scanning slices along the z -axis, either in fluorescence or DIC (differential interference contrast) mode. Cells were stained with the fluorescence cell viability kit (Molecular Probes) and imaged with the $20\times/0.75$ objective.

3. Results

3.1. Characterization of the laser beam profile

Using the knife-edge method, we established that the unfocused laser beam is well described by a Gaussian spatial profile, $\Phi(r) = \Phi_0 e^{-2r^2/\omega_0^2}$, where $\Phi(r)$ is the fluence (J/cm^2) at radial distance r in the xy plane, Φ_0 is the peak fluence, and ω_0 is the Gaussian radius of the electric field. A perfectly focused TEM₀₀ Gaussian beam also has a Gaussian profile [28] with a radius that varies with axial distance as

$$\omega(z) = \omega_0(1 + z^2/z_0^2)^{1/2}, \quad (1)$$

where the minimum radius (at $1/e^2$ of the peak intensity) is given by

$$\omega_0 = \frac{\lambda}{\pi n \tan \theta} \approx \frac{\lambda}{\pi \theta} \quad (2)$$

and the Rayleigh range is given by

$$z_0 = \frac{\lambda}{\pi \tan^2 \theta} \approx \frac{\lambda}{\pi \theta^2}. \quad (3)$$

Here $\theta = \tan^{-1}(\omega_0/z_0)$ is the divergence of the focused beam, λ is the wavelength, and n is the index of refraction. The fluence is related to the pulse energy, E , by the relation $\Phi_0(z) = 2E/\pi\omega(z)^2$.

A knife-edge scan of the beam profile at different values of z yielded $\omega(z)$, with a minimum beam radius of $2.9\ \mu\text{m}$. A least squares fit of $\omega(z)$ vs. z to Eq. (1), treating θ as a free parameter, yielded $\tan \theta = 0.229 \pm 0.005$ (in reasonable agreement with the value expected for an NA 0.25 lens), $\omega_0 = 1.11\ \mu\text{m}$, and $z_0 = 4.83\ \mu\text{m}$. The true focal radius lies somewhere between 1.1 and $2.9\ \mu\text{m}$.

We observed that an asymmetric profile is produced when the laser passes through both the beam-splitting cube and the objective lens of the assembled microscope,

with a spot size of approximately $20\ \mu\text{m}$. The beam-splitter was present in the experiments reported in the following sections, except when noted otherwise.

3.2. Ablation of collagen

Various patterns, such as the holes, lines and grids shown in Fig. 1, were produced in the collagen by manually translating the sample stage. The effects of

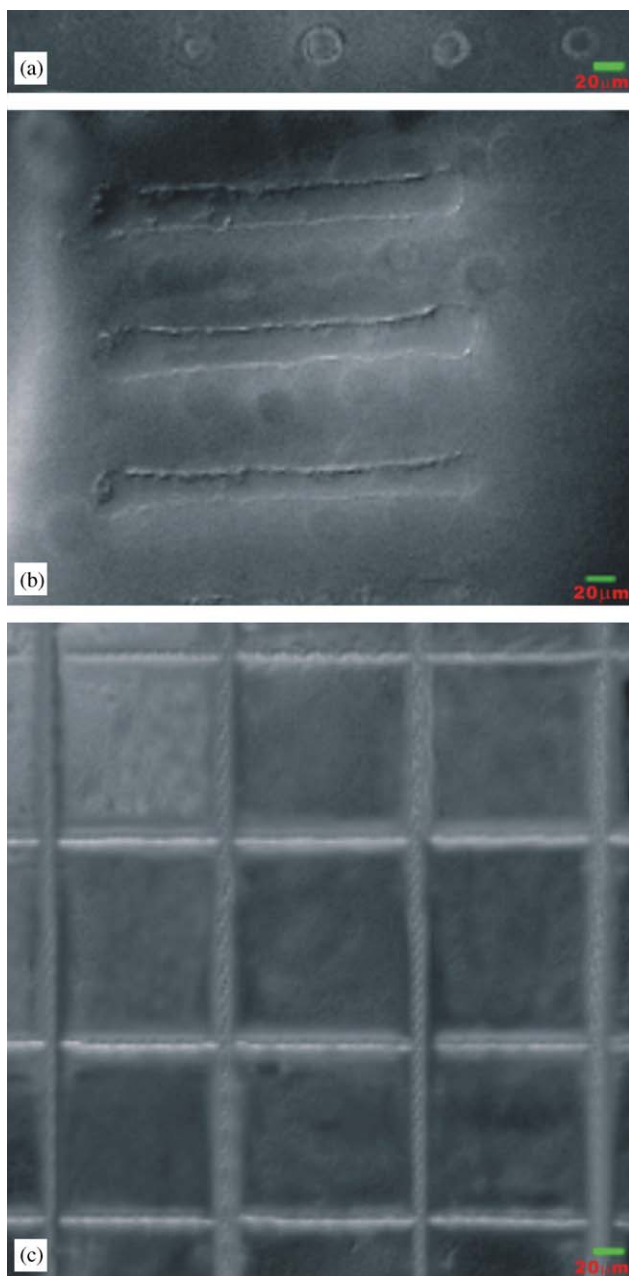


Fig. 1. DIC images of patterns generated by focusing the laser onto the collagen surface. Circular craters (a) were produced with 2 s exposures of $5.0\ \mu\text{J}/\text{pulse}$. Lines (b) were produced with $7.0\ \mu\text{J}/\text{pulse}$ and a grid pattern (c) was produced with $5.0\ \mu\text{J}/\text{pulse}$, while translating the stage at a rate of $\sim 100\ \mu\text{m}/\text{s}$. Note the scale bars of $20\ \mu\text{m}$ in each panel.

laser fluence and exposure time on the size and morphology of the ablation craters were studied systematically. Two methods were used to vary the laser fluence. In the first method (referred to as a z -scan), the pulse energy was held at a fixed value of E , and the axial distance between the objective lens and the target was varied, with negative z corresponding to the focal point lying within the sample. In the second method (referred to as an E-scan), the pulse energy was varied, while the laser was focused on the target surface, as determined visually from the optical breakdown of air.

Two z -scans were performed, one at 2.1 and the second at $7.0\ \mu\text{J}/\text{pulse}$, with an exposure time of $2.0\ \text{s}$ (2000 shots) for each value of z . The beam-splitter was removed in these measurements, so that the laser beam retained its Gaussian profile. Representative micrographs of the ablation craters produced in the $2.1\ \mu\text{J}$ scan are shown in Fig. 2. The craters taken with the focus above the surface differ qualitatively from those with the focus below the surface. The image taken at $z = +70\ \mu\text{m}$ has a very small diameter and shows little collateral damage. The image at $z = 40\ \mu\text{m}$ shows a complex damage pattern. The images at $z \leq 0$ have several common morphological features: a circular outer rim, a fairly uniform main crater, and a dark central spot. The outer rim is typically $5\text{--}10\ \mu\text{m}$ wide and is raised from the surface by $\sim 15\ \mu\text{m}$. This feature was present for all the craters with $z \leq 0$, but becomes very faint for the most negative z . The width of the outer rim was ignored in reporting the radius of the main crater. The depth of the main crater is typically $50\text{--}100\ \mu\text{m}$, although its value was not recorded systematically. The central spot, when present, is typically $5\text{--}15\ \mu\text{m}$ wide and $30\ \mu\text{m}$ deep. We also observed craters formed entirely within the bulk of the collagen, but this feature was not studied systematically.

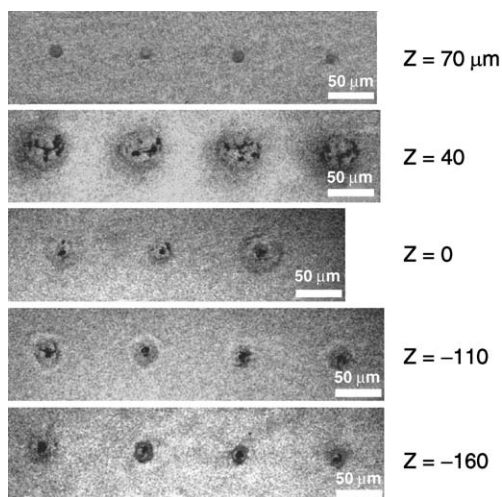


Fig. 2. Morphology of the ablation features at different locations of the laser focus. Positive z corresponds to the focus above the surface. Note the scale bars of $50\ \mu\text{m}$.

Fig. 3 shows the z -dependence of the crater diameter for both scans. These plots are markedly asymmetric, with the far-field (large $|z|$) diameters being much smaller when the focus is above the surface ($z > 0$). The upper panel of Fig. 4 shows the result of the E-scan, for a fixed irradiation time of 2.0 s. In the lower panel the pulse energy is fixed at 7.0 μJ , and the exposure time varies up to 20 s.

3.3. Cell adhesion in ablated collagen

Experiments were performed to study the adhesion and growth of cells in the ablation patterns illustrated in Fig. 1. In a first experiment, stem cells were seeded into circular craters formed by focusing the laser onto the collagen surface. Fig. 5a shows fluorescence micrographs of stem cells seeded in craters formed with a fixed pulse energy of 7.0 μJ and irradiation times ranging from 3 to 10 s. The images were taken after 7 days of incubation. The upper panel is an image taken in the xy plane; the lower panel is an image in the xz plane of the middle row of holes, reconstructed from sections taken

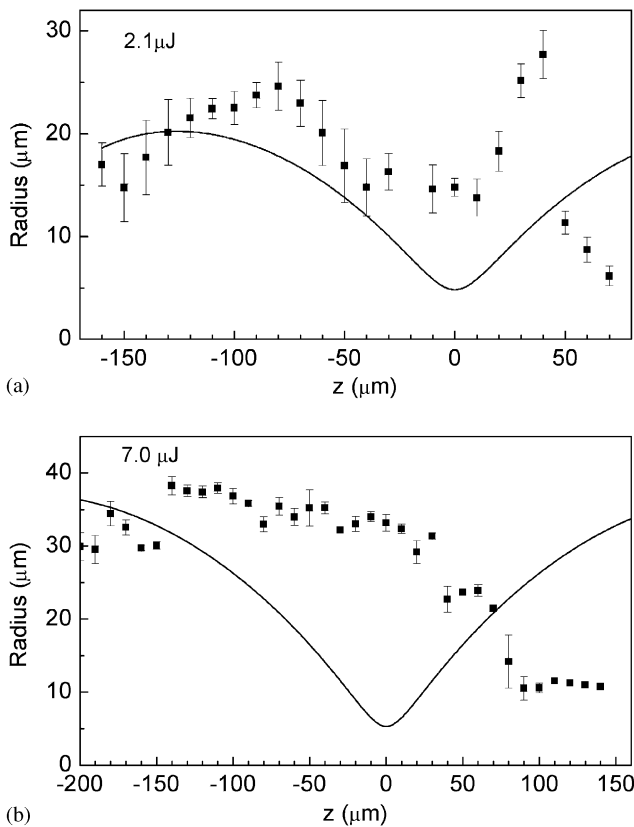


Fig. 3. Z-scan of the crater diameter for pulse energies of (a) 2.1 μJ and (b) 7.0 μJ and 2 s exposure (2000 laser shots). Each point is an average of four craters, and the error bars are a single standard deviation. The curves are defined by the optical model, Eq. (5), assuming a threshold fluence of 0.06 J/cm^2 . The model predicts that the radius should fall to zero at $z_{\text{max}} = [2E/\pi\theta^2\Phi_i]^{1/2} = 206 \mu\text{m}$ in panel (a) and $376 \mu\text{m}$ in panel (b).

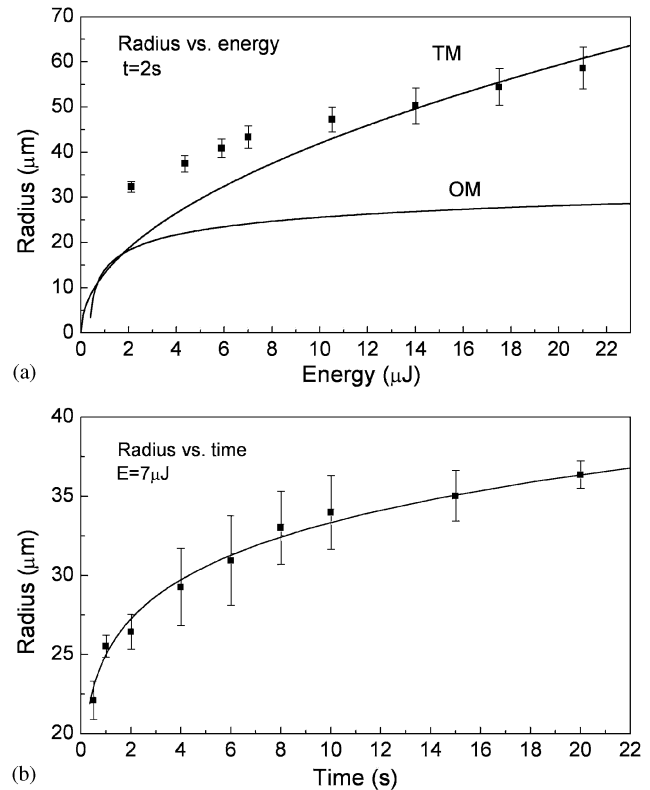


Fig. 4. Energy and time scans of the crater diameter for focusing on the collagen surface. (a) Energy scan for an irradiation time of 2 s. The curves given by the optical model (OM, Eq. (5) with $\omega_0 = 20 \mu\text{m}$) and the thermodynamic model (TM, Eq. (6)). (b) Effect of the number of laser pulses on the ablation radius for a pulse energy of 7.0 μJ . The curve is an empirical fit to a power law with an exponent of 0.125. The point in panel (a) at 7.0 μJ is somewhat smaller than the corresponding one in panel (b) at 2 s. This discrepancy may be explained by the fact that the experiments were performed with different collagen batches at slightly different focal points.

at different depths. Fig. 5b is a plot of the ablation depth determined from the lower panel of Fig. 5a. The progressively increasing penetration of the stem cells demonstrates the ability of cells to adhere at different depths of the 3D laser scaffold. In a second experiment the probability of cell attachment was measured for a set of parallel grooves (560 μm long, 70 μm wide, and 95 μm apart). We observed that the density of cells before washing the sample was uniform over the entire patterned surface, whereas after washing the cell density in the grooves was 65 times greater than on the surface. The fraction of cells trapped in the patterned grooves was estimated from the difference in cell density between the original medium and the collected medium after washing. We found that 55% of the cells in the original medium were trapped in the grooves, leaving a cell density of $1490 \text{ cells mm}^{-2}$ in the grooves. In a third experiment the viability of cells in a grid pattern was studied. The fibroblasts adhered to the original pattern after 7 days, and showed modest signs of migration after 10 days. This result is consistent with our previous

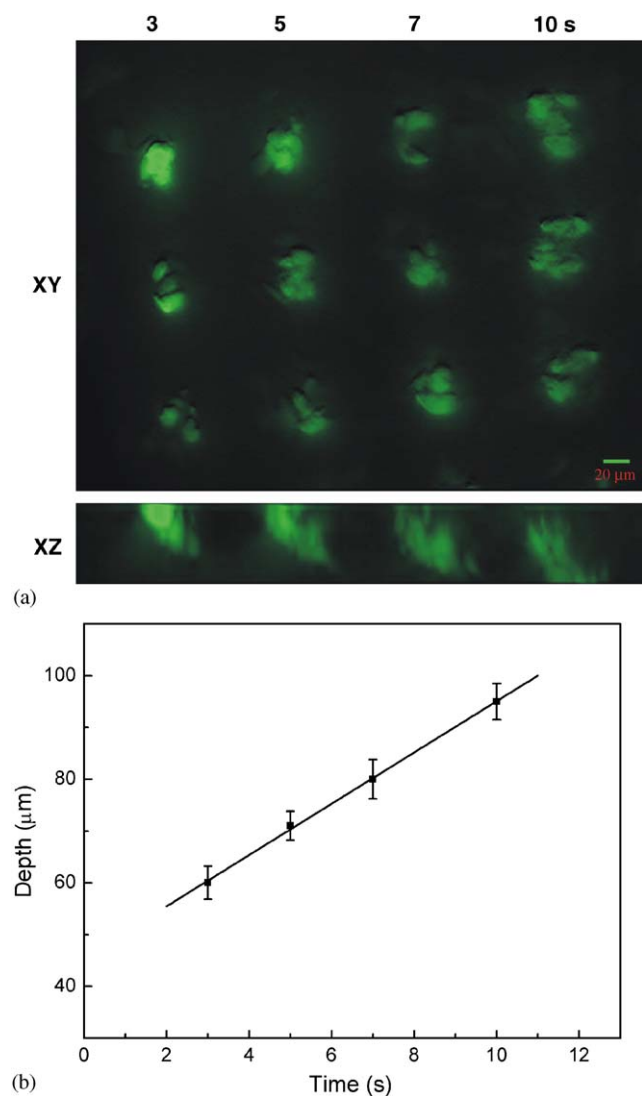


Fig. 5. Effect of exposure time on the seeding of stem cells in a 3D scaffold at a pulse energy of $7.0\mu\text{J}$. (a) Fluorescence images of holes seeded with stem cells stained with the fluorescence cell viability kit. All of the seeded cells are found to emit green fluorescence, indicating that they are viable and that their supporting matrix is biocompatible. The top three rows are superficial images of the substrate. The bottom row is a depth profile, showing that the cells penetrate further into the scaffold as the channels become deeper. Images were taken with the $20\times/0.75$ objective. Note the scale bar of $20\mu\text{m}$. (b) Depth of cell images as a function of ablation time. The line is drawn to guide the eye.

finding that cells migrate very slowly in a 3D collagen gel of a concentration $>0.6\text{mg/mL}$ [29].

More complex cell patterns were also studied. Fig. 6 shows fluorescence micrographs of fibroblasts seeded into a pattern shaped to form the letter “I”. Images of viable cells, taken after 3 days of incubation, are viewed by a dissection scan along the z axis, reconstructed to yield a 3D image of a volume $436\times 342\times 160\mu\text{m}^3$ in the three orthogonal planes. Fig. 6a (xy plane) shows the top view of the patterned cell distribution in the collagen scaffold. Figs. 6b (yz plane) and c (xz plane) show

orthotropic side views of the 3D image. The cells in these images displayed some migration after a 3 day incubation, but they were still confined within the original “I” shape of the pattern, indicating selective cell adhesion to the micropatterns. Furthermore, more than 95% of adhered cells were found viable within the patterned 3D matrix.

4. Discussion

4.1. Ablation morphology and mechanism

Because thermal damage to the scaffold may have harmful effects on cell adhesion and growth, it is important to establish the extent to which thermal effects contribute to the ablation mechanism. We consider two limiting models, which embody the opposite mechanisms of direct, photochemical ablation on one hand and thermal vaporization of the substrate on the other. The first model assumes an “optical” mechanism, in which the ablated geometry reflects the spatial profile of the laser beam. Material is assumed to be ablated before energy relaxation occurs. If Φ_t is the threshold fluence, then a Gaussian profile gives for the radius of the ablation crater

$$R = \frac{\omega(z)}{\sqrt{2}} \left[\ln \left(\frac{\Phi}{\Phi_t} \right) \right]^{1/2}. \quad (4)$$

Inserting the axial dependence of ω (Eq. (1)) yields an explicit expression for R ,

$$R = \frac{\omega_0}{\sqrt{2}} \left(1 + \frac{z^2}{z_0^2} \right)^{1/2} \left[\ln \left(\frac{\Phi_0}{\Phi_t} \right) - \ln \left(1 + \frac{z^2}{z_0^2} \right) \right]^{1/2}. \quad (5)$$

Eq. (5) shows that R initially increases with z , following the axial dependence of $\omega(z)$, reaches a maximum, and then falls to zero once $\Phi(r=0) < \Phi_t$.

In the other limit, the crater diameter is determined by the thermodynamic threshold for vaporization. In this case, R is insensitive to z unless the beam has diverged to such an extent that the energy density absorbed by the substrate is insufficient to cause vaporization. Because of the high reflectivity of the plasma, the absorbed energy is confined to a thin layer of depth δ_0 . If we make the simplifying assumption that all of the laser energy is absorbed [30] and that this energy expands to vaporize a cylinder of radius R and height δ , then the crater radius is given by

$$R = (E/\pi\delta\Delta H_v)^{1/2}, \quad (6)$$

where ΔH_v is the enthalpy of vaporization per unit volume.

Turning now to the data for the z -scans shown in Fig. 2, we need first to understand the asymmetry of R with respect to $z=0$. This effect is readily explained by

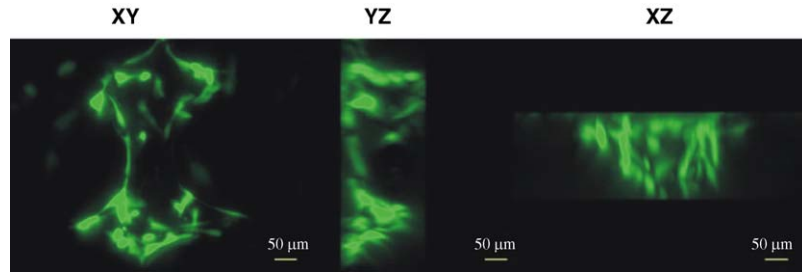


Fig. 6. Images of viable human fibroblasts viewed from the three orthogonal planes. The left panel (xy plane) represents the patterned cell distribution in the collagen scaffold when observed on the microscope stage. The middle panel (yz plane) shows the side view of the cells embedded into the patterns. The right panel (xz plane) is obtained when the viewing plane is rotated 90° about the xz plane. The original pattern of the capital letter “I” was sharply defined. These images, recorded after a 3-day incubation, suggest that the extent of cell migration was limited. Note the scale of bar of $50\ \mu\text{m}$.

the fact that when the laser is focused above the surface, breakdown of the air shields the substrate, and the reduced fluence leads to a much smaller ablation radius. The very small craters at $z = 70\ \mu\text{m}$ indicate extensive shielding, whereas the very complex pattern of destruction at $40\ \mu\text{m}$ could be the result of the airborne plasma interacting with the surface below. The outer rims observed for $z \leq 0$ are very likely caused by the outward flow of molten material, which is an additional source of thermal damage [31]. The deep, central feature observed at higher fluences may be caused by self-focusing of the laser beam, an effect that has been observed in water [30] and gelatin [32]. The critical power for self-focusing in water is $2.5\ \text{MW}$ [33], which is well below the level used in the present experiments.

Considering now the data for $z < 0$, we see in Fig. 3b that at $E = 7.0\ \mu\text{J}$ the ablation radius depends only weakly on z and generally exceeds the optical value. It thus appears that for this pulse energy the mechanism is largely thermal. For $E = 2.1\ \mu\text{J}$, there is a pronounced maximum in $R(z)$ at $z = -80\ \mu\text{m}$, indicative of the optical mechanism.

In order to place these observations on a more quantitative footing, we replotted the data in Fig. 7 in reduced form, displaying $R(z)/\omega(z)$ as a function of $\Phi(z)/\Phi_t$. A least squares fit of the data for $z < 0$ in the region $\Phi/\Phi_t \leq 5$ yields a value of $\Phi_t = 0.062 \pm 0.06\ \text{J}/\text{cm}^2$ for the threshold fluence. We note that R/ω for $z > 0$ lies entirely below the model curve in the far field, as would be expected for plasma shielding. The data for $z < 0$ fall into three regions. The ablation radii for and $\Phi(z)/\Phi_t < 5$ lie close to the optical model (Fig. 7a), providing an accurate measure of the threshold. The near absence of crater rims indicates very little collateral damage in this regime. For $5 < \Phi(z)/\Phi_t < 20$, the ablation radius follows the optical model but lies above the curve. The presence of a crater rim is indicative of some collateral melting. For $\Phi(z)/\Phi_t > 20$, the ablation radius diverges strongly from the optical model, showing clearly the dominance of the thermal mechanism in this regime.

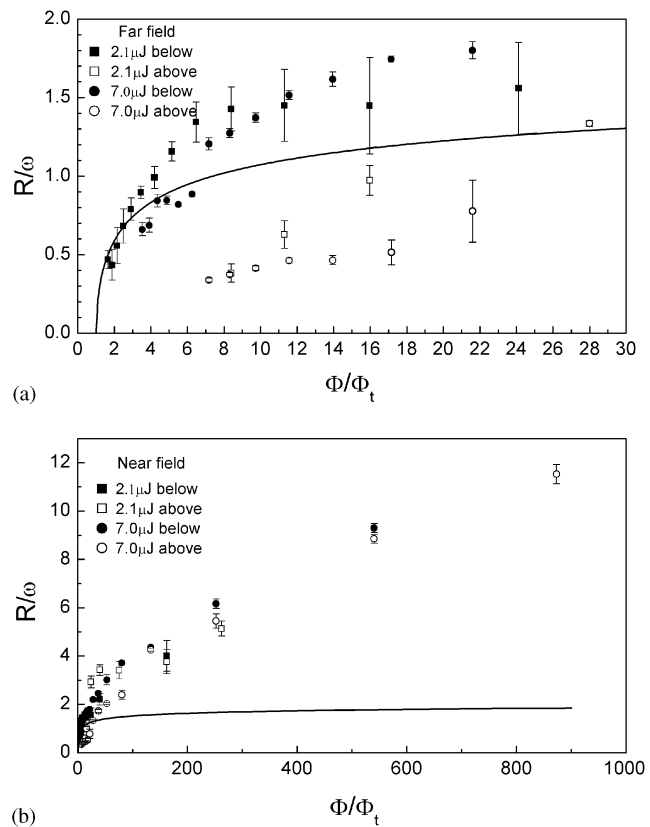


Fig. 7. Reduced dimension plot of the z -scans, showing (a) threshold behavior in the far field and (b) high fluence behavior in the near field. Squares denote the $2.1\ \mu\text{J}$ scan and circles denote the $7.0\ \mu\text{J}$ scan. Solid symbols are for the focal point within the sample, and open symbols are for the focus above the sample. The curves are the prediction of the optical model (Eq. (5)).

These results are supported by the E-scan data. Assuming an ω_0 value of $20\ \mu\text{m}$ in Fig. 5a (these data were taken with the beam-splitter in place), the fluence ratio Φ/Φ_t ranges from 8.0 to 80, extending into the range for thermal ablation. We find that the data are described qualitatively by Eq. (6), assuming $\Delta H_v = 2580\ \text{J}/\text{cm}^3$ (the enthalpy density for vaporization of water at 25°C) and a fitted value of $\delta = 0.7\ \mu\text{m}$.

We also examined the effects of multiple laser shots. Fig. 4b shows that the crater radius increases with exposure time according to an empirical power law, $R = At^n$, with $n = 0.125 \pm 0.010$. There have been many studies of the cumulative effects of multiple laser pulses on surface damage in a wide variety of materials [34]. It has been shown that the damage threshold for a pulse train lies below that for a single pulse and that the single-pulse threshold decreases with bulk temperature. A variety of mechanisms have been proposed to explain the multipulse effect, including photochemical bond-breaking and thermal heating [34]. The mechanism here is complicated by the fact that as the crater becomes deeper the rate of energy absorption slows down because of plasma shielding. A plausible explanation of Fig. 4b is that the collagen surface temperature increases with the number of laser pulses. Assuming that Φ_t decreases with temperature, the optical model predicts an increase in the ablation radius with exposure time. The observed growth in R as the exposure time is increased from 0.5 to 20 s corresponds to a reduction in Φ_t by a factor of 5.

It is useful to compare our results with two previous studies of fs ablation of collagen. Oraevsky et al. [35] used single shots of a mildly focused 1053 nm laser, with a pulse energy of 4.4 mJ, pulse durations between 300 fs and 1 ns, and a spot size of 500 μm . Their study showed that the shortest pulses produced a higher ablation efficiency, with less thermal damage and recoil stress. The ablated features for $\Phi/\Phi_t = 2.2$ were approximately the same size as the laser beam and showed little collateral damage. Our measured damage threshold at 50 fs is in quantitative agreement with an extrapolation of their data. In another study, Smith et al. [36] used very long ($\sim 10^6$ – 10^{10}) pulse trains of 775 nm radiation generated by a Ti:Sapphire oscillator, with 80 fs pulse width, 82 MHz repetition rate, and a typical pulse energy of 0.1 nJ. The laser beam was tightly focused with a focal spot size estimated to be 0.5 μm . Close to threshold with different amounts of added dye, the ablated features were approximately the same width as the laser spot size. Ablation features were created in 3D layers down to 30 μm beneath the surface, with little apparent thermal damage. Our findings are consistent with the previous studies but cover a much broader range of laser fluence.

4.2. Cell growth in laser patterned collagen

It is well known that surface microtopography and chemistry are critical for cell viability. For example, Duncan et al. [20] studied the adhesion of osteoprogenitor cells on Mylar disks ablated with 248 nm excimer laser radiation (20 ns pulse width). They found that the cells grew preferentially in grooves with smooth surfaces having minimal width and depth, and saw no cell

orientation effects. They could not distinguish between physical and chemical effects on cell adhesion. Schwarz et al. [37] found that 193 nm excimer radiation enhanced biomolecule adsorption on polymer surfaces as a result of increased surface roughness and greater hydrophobicity, the latter arising from an increased carbon/oxygen ratio at the surface. In contrast, Ertel et al. [38] found that surface carbonyl groups (i.e., a reduced C/O ratio) enhanced the growth of bovine aortic endothelial cells. Duncan et al. [20] speculated that carbon deposition on the surface caused by the laser plume inhibits cell adhesion.

In the present case we believe that mechanical trapping in the ablation pattern is the primary mechanism for cell adhesion, as evidenced by the observation that cells in the patterned grooves are 65 times more likely to survive washing of the sample as compared with cells on the surface. Although we did not find any effects of groove dimensions on cell adhesion, in a related study [39] we observed that the cell orientation is affected by the shape of the ablation pattern. In addition, it is possible that photochemical changes produced on the surface by the ultrafast laser may play a role. Further studies of the ablated surface chemistry and morphology are warranted.

5. Conclusions

The main new result of this paper is that collagen features sculpted in the intermediate fluence regime are hospitable to cell adhesion and growth in 3D. Both rat mesenchymal stem cells and human fibroblasts seeded in the collagen scaffold remained viable for several days and showed little mobility outside of the micropattern. We established that the damage threshold is $0.062 \pm 0.06 \text{ J/cm}^2$ for 50 fs pulses at 800 nm (for 2 s exposure at 1 kHz repetition rate). An optical model describes the ablation for fluences up to 5 times the threshold with no collateral damage and with only minor damage up to 20 times this value. At higher fluence the ablation features are produced primarily by a thermal mechanism.

Acknowledgments

We wish to thank the Campus Research Board of the University of Illinois at Chicago for partial support of this research. In addition, RJG acknowledges support from the NSF under grants nos. PHY 0200812 and CHE 0120997, and MRC acknowledges support from the NIH (GM60741). We also wish to thank Dr. Jeremy Mao of the Department of Orthodontics at UIC for providing us with rat mesenchymal stem cells, and Joel Wise, Vladimir Skavysh, and Brian Connolly for their assistance with some of the experiments.

References

- [1] Yang S, Leong K, Du Z, Chua C. The design of scaffolds for use in tissue engineering, part I, traditional factors. *Tissue Eng* 2001;7:679–89.
- [2] Wang JH, Jia F, Gilbert TW, Woo SL. Cell orientation determines the alignment of cell-produced collagenous matrix. *J Biomech* 2003;36:97–102.
- [3] Gudjonsson T, Ronnov-Jessen L, Villadsen R, Bissell MJ, Petersen OW. To create the correct microenvironment: three-dimensional heterotypic collagen assays for human breast epithelial morphogenesis and neoplasia. *Methods* 2003;30:247–55.
- [4] Pachence JM. Collagen-based devices for soft tissue repair. *Biomed Mater Res* 1996;33:35–40.
- [5] Folch A, Toner M. Microengineering of cellular interactions. *Annu Rev Biomed Eng* 2000;2:227–56.
- [6] Kane RS, Takayama S, Ostuni E, Ingber DE, Whitesides GM. Patterning proteins and cells using soft lithography. *Biomaterials* 1999;20:2363–76.
- [7] Vozzi G, Flaim C, Ahluwalia A, Bhatia S. Fabrication of PLGA scaffolds using soft lithography and microsyringe deposition. *Biomaterials* 2003;24:2533–40.
- [8] Tan W, Desai TA. Microfluidic patterning of cells in extracellular matrix biopolymers: effects of channel size, cell type, and matrix composition on pattern integrity. *Tissue Eng* 2003;9:255–67.
- [9] Tan W, Desai TA. Microfluidic patterning of cellular biopolymer matrices for biomimetic 3-D structures. *Biomed Microdevices* 2003;3:234–44.
- [10] Tan W, Krishnaraj R, Desai TA. Evaluation of nanostructured composite collagen–chitosan matrices for tissue engineering. *Tissue Eng* 2001;7:203–10.
- [11] Anderson JR, Chiu DT, Jackman RJ, Cherniavskaya O, McDonald JC, Wu H, Whitesides SH, Whitesides GM. Fabrication of topologically complex three-dimensional microfluidic systems in PDMS by rapid prototyping. *Anal Chem* 2000;72:3158–64.
- [12] Chiu DT, Jeon NL, Huang S, Kane RS, Wargo CJ, Choi IS, Ingber DE, Whitesides GM. Patterned deposition of cells and proteins onto surfaces by using three-dimensional microfluidic systems. *Proc Natl Acad Sci* 2000;97:2408–13.
- [13] Piner RD, Zhu J, Xu F, Hong S, Mirkin CA. “Dip-Pen” nanolithography. *Science* 1999;283:661–3.
- [14] Odde DJ, Renn MJ. Laser-guided direct writing for applications in biotechnology. *Trends Biotechnol* 1999;7:385–9.
- [15] Veissh M, Wickes BT, Castner DG, Zhang M. Guided cell patterning on gold-silicon dioxide substrates by surface molecular engineering. *Biomaterials* 2004;25:3315–24.
- [16] Roth EA, Xu T, Das M, Gregory C, Hickman JJ, Boland T. Inkjet printing for high-throughput cell patterning. *Biomaterials* 2004;25:3707–15.
- [17] Joglekar AP, Liu H, Spooner GJ, Meyhofer E, Mourou G, Hunt AJ. A study of the deterministic character of optical damage by femtosecond laser pulses and applications to nanomachining. *Appl Phys B—Lasers Opt* 2003;77:25–30.
- [18] Vogel A, Venugopalan V. Mechanisms of pulsed laser ablation of biological tissues. *Chem Rev* 2003;103:577–644.
- [19] Thissen H, Hayes JP, Kingshott P, Johnson G, Harvey EC, Griesser HJ. Nanometer thickness laser ablation for spatial control of cell attachment. *Smart Mater Struct* 2002;11:792–9.
- [20] Duncan AC, Weisbuch F, Rouais F, Lazare S, Baquey Ch. Laser microfabricated model surfaces for controlled cell growth. *Biosens Bioelectron* 2002;17:413–26.
- [21] Vaidya R, Tender LM, Bradley G, O’Brien 2nd MJ, Cone M, Lopez GP. Computer-controlled laser ablation: a convenient and versatile tool for micropatterning biofunctional synthetic surfaces for applications in biosensing and tissue engineering. *Biotechnol Prog* 1998;14:371–7.
- [22] Stuart BC, Feit MD, Herman S, Rubenchik AM, Shore BW, Perry MD. Nanosecond to femtosecond laser-induced breakdown in dielectrics. *Phys Rev B* 1996;53:1749–61.
- [23] Lubatschowski H, Maat G, Heisterkamp A, Hetzel U, Drommer W, Welling H, Ertmer W. Application of ultrashort laser pulses for intrastomal refractive surgery. *Graefes Arch Clin Exp Ophthalmol* 2000;238:33–9.
- [24] Tsai PS, Friedman B, Ifarraguerri AI, Thompson BD, Lev-Ram V, Schaffer CB, Xiong Q, Tsien RY, Squier JA, Kleinfeld D. All-optical histology using ultrashort laser pulses. *Neuron* 2003;39:27–41.
- [25] Schaffer CB, Brodeur A, Mazur E. Laser-induced breakdown and damage in bulk transparent materials induced by tightly focused femtosecond laser pulses. *Meas Sci Technol* 2001;12:1784–94.
- [26] Petite H, Duval J, Frei V, Abdul-Malak N, Sigot-Luizard M, Herbage D. Cytocompatibility of calf pericardium treated by glutaraldehyde and by the acyl azide methods in an organotypic culture model. *Biomaterials* 1995;16:1003–6.
- [27] Hey KB, Laths CM, Raxworthy MJ, Wood EJ. Crosslinked fibrous collagen for use as a dermal implant: control of the cytotoxic effects of glutaraldehyde and dimethylsuberimidate. *Biotechnol Appl Biochem* 1990;12:85–93.
- [28] Yariv A. *Quantum electronics*, 2nd ed. NY: Wiley; 1989.
- [29] Sun S, Wise J, Cho MR. Human fibroblast migration in three-dimensional collagen gel in response to noninvasive electrical stimulus I. characterization of induced three-dimensional cell movement. *Tissue Eng* 2004;10(9/10):1548–56.
- [30] Vogel A, Noack J, Nahen K, Theisen D, Busch S, Parltz U, Hammer DX, Noojin GD, Rockwell BA, Birngruber R. Energy balance of optical breakdown in water at nanosecond to femtosecond time scales. *Appl Phys B* 1999;68:271–80.
- [31] Frenz M, Romano V, Zweig AD, Weber HP, Chapliev NI, Silenok AV. Instabilities of laser cutting of soft media. *J Appl Phys* 1989;64:496–503.
- [32] Maatz G, Heisterkamp A, Lubatschowski H, Barcikowski S, Fallnich C, Welling H, Ertmer W. Chemical and physical side effects at application of ultrashort laser pulses for intrastomal refractive surgery. *J Opt A—Pure Appl Opt* 2000;2:59–64.
- [33] Feng Q, Moloney JV, Newell AC, Wright EM, Cook K, Kennedy PK, Hammer DX, Rockwell BA, Thompson CR. Theory and simulation on the threshold of water breakdown induced by focused ultrashort laser pulses. *IEEE Quant Electron* 1997;33:127–37.
- [34] Chmel AE. Fatigue laser-induced damage in transparent materials. *Mater Sci Eng B* 1997;49:175–90.
- [35] Oraevsky AA, Da Silva LB, Rubenchik AM, Feit MD, Glinesky ME, Perry MD, Mammini BM, Small W, Stuart BC. Plasma mediated ablation of biological tissues with nanosecond-to-femtosecond laser pulses: relative role of linear and nonlinear absorption. *IEEE J Selected Topics Quant Elect* 1996;2:801–9.
- [36] Smith NI, Fujita K, Nakamura O, Kawata S. Three-dimensional subsurface microprocessing of collagen by ultrashort laser pulses. *Appl Phys Lett* 2001;78:999–1001.
- [37] Schwarz A, Rossier JS, Roulet E, Mermod N, Roberts MA, Girault HH. Micropatterning of biomolecules on polymer substrates. *Langmuir* 1998;14:5526–31.
- [38] Ertel SI, Chilkoti A, Horbett TA, Ratner BD. Endothelial cell growth on oxygen-containing films deposited by radio-frequency plasmas: the role of surface carbonyl groups. *J Biomater Sci Polym Ed* 1991;3:163–83.
- [39] Sun S, Liu Y, Singha S, Gordon RJ, Cho MR. Behavior of rat mesenchymal stem cells in micropatterned biopolymers with an ultrafast pulsed laser, submitted for publication.